

# Thermal Conductivity Predictions with Foundation Atomistic Models

Balázs Póta,<sup>1</sup> Paramvir Ahlawat,<sup>1</sup> Gábor Csányi,<sup>2</sup> and Michele Simoncelli<sup>1,\*</sup>

<sup>1</sup>*Theory of Condensed Matter Group of the Cavendish Laboratory, University of Cambridge, Cambridge, UK*  
<sup>2</sup>*Engineering Laboratory, University of Cambridge, Cambridge, UK*

Recent advances in machine learning have led to foundation models for atomistic materials chemistry, potentially enabling quantum-accurate descriptions of interatomic forces at reduced computational cost. These models are benchmarked by predicting materials' properties over large databases; however, these computationally intensive tests have been limited to basic quantities related to harmonic phonons, leaving uncertainty about the reliability for complex, technologically and experimentally relevant anharmonic heat-conduction properties. Here we present an automated framework that relies on foundation models to compute microscopic vibrational properties, and employs them within the Wigner formulation of heat transport to predict the macroscopic thermal conductivity in solids with arbitrary composition and structure. We apply this framework with the foundation models M3GNet, CHGNet, MACE-MP-0, and SevenNET to 103 diverse compounds, comparing predictions against first-principles references and introducing a benchmark metric based on conductivity. This framework paves the way for physics-aware, accurate predictions of vibrational and thermal properties, and for uncovering materials that violate semiclassical Boltzmann transport and feature exceptional heat-shielding or thermoelectric performance.

Over the past decades, several research groups have tackled the challenging computational task of fitting the Born-Oppenheimer potential energy surface as a function of atomic coordinates [1–7]. These efforts resulted in the development of so-called machine-learning potentials (MLPs), which allow us to reproduce first-principles energies and microscopic interatomic forces with nearly the same accuracy and orders-of-magnitude lower computational cost. These developments enable the prediction of macroscopic observables from the integration of atomistic properties at a computational cost much reduced compared to first-principles methods, effectively opening avenues to design materials for target applications from theory. For example, engineering the magnitude of the macroscopic thermal conductivity of a material through changes in its atomistic composition and structure is crucial for neuromorphic computing [8], thermoelectric energy harvesting [9], and aerospace [10] technologies. Major drawbacks of MLPs-based methods are the significant work required to generate a first-principles database used to train and validate MLPs [11], as well as the applicability limited to specific materials' compositions or structural phases. Past works attempted to bypass these limitations by employing end-to-end machine-learning methods, which predict microscopic [12] or macroscopic [13, 14] materials' properties very efficiently, but with the compromise of not rigorously resolving the fundamental physics that underlies them. Fittingly, recent work [15] has formally demonstrated the possibility to obtain a complete description (in the mathematical sense) of atomic environments (and thus of forces) by employing Message Passing Neural Networks (MPNNs) models [16] with many-body messages [17] (to be precise, with the MACE architecture [17] this can be achieved using 4-body terms and one message pass). This breakthrough has enabled the development of foundation

machine-learning potentials (fMLPs) [18–23], which are trained across nearly all chemical elements and can be directly combined to describe materials with diverse structures and compositions. Therefore, fMLPs could potentially overcome the problems related to complex training and the very limited transferability of conventional MLPs, ultimately enabling physics-aware predictions of macroscopic observables from the integration of atomistic quantities. Recent research efforts have assessed the accuracy of fMLPs in predicting, e.g., the structural stability of solids [24] or the harmonic vibrational frequencies [25–28]. However, fMLPs have not yet been tested for predicting vibrational-anharmonic and heat-conduction properties, due to the complexity of the computational framework that relates the interatomic forces to the macroscopic conductivity [29–37].

Here we present an automated framework that uses fMLPs to compute anharmonic vibrational and thermal properties. We employ this to benchmark against first-principles reference data [30, 31] the predictions obtained from state-of-the-art (SOTA) fMLPs M3GNet [18], CHGNet [19], MACE-MP-0 [20], and SevenNET [21] (all trained on the Materials Project DFT-PBE database [38] and hereafter collectively referred to as 'mp-fMLPs'). In particular, after detailing the methods to calculate harmonic and anharmonic vibrational properties of solids using fMLPs, we discuss how these quantities determine the thermal conductivity within the recently developed Wigner heat-Transport Equation (WTE) [34, 35], which generalizes the Boltzmann Transport Equation (BTE) [39] accounting not only for heat carried by particle-like propagation of phonons, but also for conduction arising from phonons' wave-like tunneling. Thus, this framework is employed to predict from DFT-PBE or mp-fMLPs the thermal conductivity of 103 compounds made up of 34 different chemical species and

having wurtzite, zincblende, or rocksalt structure. We introduce descriptors to quantify the accuracy of fMLPs in predicting anharmonic and thermal properties, and show that they could potentially be used as a metric to benchmark or fine-tune fMLPs. Finally, we show how the framework introduced paves the way for rigorous, physics-aware predictions of vibrational and thermal properties in materials with arbitrary composition and structure, highlighting its potential to find materials that violate semiclassical Boltzmann conduction relevant for thermal-insulation or thermoelectric applications.

## Results

### From vibrational energy to thermal conductivity

The temperature-dependent thermal conductivity ( $\kappa(T)$ ) of a solid is a macroscopic, experimentally and technologically relevant quantity that describes the capability to conduct heat. To predict such quantity, we start from the Born-Oppenheimer Hamiltonian for atomic vibrations [35] expanded up to anharmonic third order in displacements from equilibrium, and we account for kinetic-energy perturbations due to isotopes [40],

$$\begin{aligned} \hat{H} = & \sum_{\mathbf{R}, b, \alpha} \frac{\hat{p}_{\mathbf{R}b\alpha}^2}{2M_b} + \frac{1}{2} \sum_{\substack{\mathbf{R}, b, \alpha \\ \mathbf{R}', b', \alpha'}} \frac{\partial^2 V}{\partial u_{\mathbf{R}b\alpha} \partial u_{\mathbf{R}'b'\alpha'}} \Big|_{\text{eq}} u_{\mathbf{R}b\alpha} u_{\mathbf{R}'b'\alpha'} \\ & + \frac{1}{3!} \sum_{\substack{\mathbf{R}, b, \alpha \\ \mathbf{R}', b', \alpha'}} \frac{\partial^3 V}{\partial u_{\mathbf{R}b\alpha} \partial u_{\mathbf{R}'b'\alpha'} \partial u_{\mathbf{R}''b''\alpha''}} \Big|_{\text{eq}} u_{\mathbf{R}b\alpha} u_{\mathbf{R}'b'\alpha'} u_{\mathbf{R}''b''\alpha''} \\ & + \sum_{\mathbf{R}, b, \alpha} \left( \frac{m_b}{M_b} - 1 \right) \frac{\hat{p}_{\mathbf{R}b\alpha}^2}{2M_b}, \end{aligned} \quad (1)$$

where  $\hat{p}_{\mathbf{R}b\alpha}$  and  $\hat{u}_{\mathbf{R}b\alpha}$  are the momentum and positions-displacement operators along the Cartesian direction  $\alpha$  for the atom  $b$  having isotope-averaged mass  $M_b$  and position  $\mathbf{R}+\tau_b$  (here,  $\mathbf{R}$  is the Bravais-lattice vector and  $\tau_b$  the position in the crystal's primitive cell); the last term in Eq. (1) describes kinetic-energy perturbations induced by isotopes [29, 40] ( $m_b$  is the exact mass of the atom at position  $\tau_b$ , which can deviate from the isotopically-averaged mass  $M_b$ ). The leading (harmonic) term in such an equation determines the vibrational frequencies; in particular, the Fourier transform of the mass-rescaled second-order derivative of the interatomic potential yields the dynamical matrix at wavevector  $\mathbf{q}$ ,  $D(\mathbf{q})_{ba,b'\alpha'} = \sum_{\mathbf{R}} \frac{\partial^2 V}{\partial u_{\mathbf{R}ba} \partial u_{\mathbf{R}'b'\alpha'}} \Big|_{\text{eq}} \frac{e^{-i\mathbf{q}\cdot(\mathbf{R}+\tau_b-\tau_{b'})}}{\sqrt{M_b M_{b'}}}$ . By diagonalizing the dynamical matrix,

$$\sum_{b'\alpha'} D(\mathbf{q})_{ba,b'\alpha'} \mathcal{E}(\mathbf{q})_{s,b'\alpha'} = \omega^2(\mathbf{q})_s \mathcal{E}(\mathbf{q})_{s,ba}, \quad (2)$$

one obtains from the eigenvalues the phonon energies  $\hbar\omega(\mathbf{q})_s$  of the solid ( $s$  is a band index ranging from 1 to  $3N_{\text{at}}$ , where  $N_{\text{at}}$  is the number of atoms in the primitive cell), and from the eigenvectors  $\mathcal{E}(\mathbf{q})_{s,ba}$  the displacement patterns of atom  $b$  in direction  $\alpha$  for the normal mode  $s$ .

The third derivative in Eq. (1), instead, determines the anharmonic linewidth  $\hbar\Gamma_a(\mathbf{q})_s$  (energy broadening due to three-phonon interactions [29]) of the phonon  $(\mathbf{q})_s$ :

$$\begin{aligned} \hbar\Gamma_a(\mathbf{q})_s = & \frac{\pi}{N_c^2} \sum_{\substack{\mathbf{q}', \mathbf{q}'' \\ s', s''}} \left\{ 2[\bar{N}(\mathbf{q}')_{s'} - \bar{N}(\mathbf{q}'')_{s''}] \delta(\omega(\mathbf{q})_s + \omega(\mathbf{q}')_{s'} - \omega(\mathbf{q}'')_{s''}) \right. \\ & \left. + [1 + \bar{N}(\mathbf{q}')_{s'} + \bar{N}(\mathbf{q}'')_{s''}] \delta[\omega(\mathbf{q})_s - \omega(\mathbf{q}')_{s'} - \omega(\mathbf{q}'')_{s''}] \right\} \times \\ & \left| \sum_{\substack{\alpha, \alpha', \alpha'' \\ b, b', b'', \mathbf{R}' \mathbf{R}''}} \frac{\partial^3 V}{\partial u_{\mathbf{R}b\alpha} \partial u_{\mathbf{R}'b'\alpha'} \partial u_{\mathbf{R}''b''\alpha''}} \mathcal{E}(\mathbf{q})_{s,ba} \mathcal{E}(\mathbf{q}')_{s',b'\alpha'} \mathcal{E}(\mathbf{q}'')_{s'',b''\alpha''} \right. \\ & \left. \sqrt{\frac{\hbar^3}{8} \frac{\Delta(\mathbf{q} + \mathbf{q}' + \mathbf{q}'') e^{-i[\mathbf{q}\cdot\tau_b + \mathbf{q}'\cdot(\mathbf{R}' + \tau_{b'}) + \mathbf{q}''\cdot(\mathbf{R}'' + \tau_{b''])]}}{\sqrt{M_b M_{b'} M_{b''} \omega(\mathbf{q})_s \omega(\mathbf{q}')_{s'} \omega(\mathbf{q}'')_{s''}}}} \right|^2, \end{aligned} \quad (3)$$

where  $\bar{N}(\mathbf{q})_s = [\exp(\hbar\omega(\mathbf{q})_s/k_B T) - 1]^{-1}$  is the Bose-Einstein distribution at temperature  $T$ ,  $\Delta(\mathbf{q} + \mathbf{q}' + \mathbf{q}'')$  is the Kronecker delta (equal to 1 if  $\mathbf{q} + \mathbf{q}' + \mathbf{q}''$  is a reciprocal lattice vector, zero otherwise),  $\delta$  is the Dirac delta. The last line in Eq. (1) accounts for the presence of isotopic-mass disorder and yields the following linewidth [40]

$$\begin{aligned} \hbar\Gamma_i(\mathbf{q})_s = & \frac{\hbar\pi}{2N_c} [\omega(\mathbf{q})_s]^2 \sum_{\mathbf{q}', s'} \delta[\omega(\mathbf{q})_s - \omega(\mathbf{q}')_{s'}] \\ & \times \sum_b g_2^b \left| \sum_{\alpha} \mathcal{E}(\mathbf{q})_{s,ba}^* \mathcal{E}(\mathbf{q}')_{s',ba} \right|^2, \end{aligned} \quad (4)$$

where  $g_2^b = \sum_i f_{i,b} \left( \frac{M_b - m_{i,b}}{M_b} \right)^2$  describes the variance the isotopic masses of atom  $b$  ( $f_{i,b}$  and  $m_{i,b}$  are the mole fraction and mass, respectively, of the  $i$ th isotope of atom  $b$ ;  $M_b = \sum_i f_{i,b} m_{i,b}$  is the weighted average mass).

The recently developed WTE [34, 35] allows to predict the thermal conductivity of solids accounting for the interplay between structural disorder, anharmonicity, and Bose-Einstein statistics of vibrations. This offers a comprehensive approach to describe ordered ‘simple crystals’ having phonon interband spacings much larger than the linewidths [41, 42], completely disordered glasses [36, 43, 44], as well as the intermediate regime of ‘complex crystals’ with interband spacings smaller than the linewidths [35, 45, 46]. To assess how the accuracy in the prediction of the conductivity is affected by the precision with which fMLPs describe harmonic and anharmonic (third-order) force constants in Eq. (1), it is sufficient to consider the conductivity obtained from the WTE solved in the single-mode relaxation-time approximation (SMA)

$$\begin{aligned} \kappa(T) = & \frac{1}{\mathcal{V} N_c} \sum_{\mathbf{q}, s} C(\mathbf{q})_s \frac{\|\mathbf{v}(\mathbf{q})_{s,s}\|^2}{3} [\Gamma(\mathbf{q})_s]^{-1} \\ & + \frac{1}{\mathcal{V} N_c} \sum_{\mathbf{q}, s \neq s'} \frac{\omega(\mathbf{q})_s + \omega(\mathbf{q})_{s'}}{4} \left[ \frac{C(\mathbf{q})_s}{\omega(\mathbf{q})_s} + \frac{C(\mathbf{q})_{s'}}{\omega(\mathbf{q})_{s'}} \right] \frac{\|\mathbf{v}(\mathbf{q})_{s,s'}\|^2}{3} \\ & \times \frac{\frac{1}{2} [\Gamma(\mathbf{q})_s + \Gamma(\mathbf{q})_{s'}]}{\left[ \omega(\mathbf{q})_s - \omega(\mathbf{q})_{s'} \right]^2 + \frac{1}{4} [\Gamma(\mathbf{q})_s + \Gamma(\mathbf{q})_{s'}]^2}; \end{aligned} \quad (5)$$

where  $C(\mathbf{q})_s = \frac{\hbar^2 \omega^2(\mathbf{q})_s}{k_B T^2} \bar{N}(\mathbf{q})_s [\bar{N}(\mathbf{q})_s + 1]$  is the specific heat of the vibration with energy  $\omega(\mathbf{q})_s$  and total linewidth  $\Gamma(\mathbf{q})_s = \Gamma_a(\mathbf{q})_s + \Gamma_i(\mathbf{q})_s$ ,  $v^\beta(\mathbf{q})_{s,s'} = \sum_{b,\alpha,b',\alpha'} \mathcal{E}^*(\mathbf{q})_{s,b\alpha} [\nabla_\mathbf{q}^\beta \sqrt{D(\mathbf{q})}_{b\alpha,b'\alpha'}] \mathcal{E}(\mathbf{q})_{s',b'\alpha'}$  is the velocity operator coupling eigenstates  $s$  and  $s'$  at the same wavevector  $\mathbf{q}$  (its diagonal elements  $s = s'$  are the usual phonon group velocities) [35],  $N_c$  is the number of  $\mathbf{q}$ -points used to sample the Brillouin zone and  $\mathcal{V}$  is the crystal's primitive-cell volume. The first line on the right-hand side of Eq (5) describes a conduction mechanism in which vibrations carry the heat  $C(\mathbf{q})_s$  by propagating particle-like with velocity  $\mathbf{v}(\mathbf{q})_{s,s}$  over the lifetime  $[\Gamma(\mathbf{q})_s]^{-1}$ . It can be rigorously shown [34, 35] that it coincides with the conductivity emerging from the Peierls-Boltzmann equation [39], and will be henceforth referred to as  $\kappa_p$ . The term on the second and third lines of Eq. (5) accounts for conduction through a wave-like tunneling mechanism between pairs of vibrational eigenstates. This term arises from the coherence between two different phonon modes  $s, s'$  at the same wavevector  $\mathbf{q}$  (*i.e.*, it becomes more significant as their frequency difference  $\omega(\mathbf{q})_s - \omega(\mathbf{q})_{s'}$  becomes smaller) and is therefore referred to as ‘coherences conductivity’,  $\kappa_c$ . It has been shown in Refs. [34, 35, 47] that in simple crystals  $\kappa_p \gg \kappa_c$  because particle-like propagation dominates over the wave-like tunneling. In contrast, in complex crystals both these mechanisms co-exist and can have comparable magnitude, implying  $\kappa_p \sim \kappa_c$ . Finally, Refs. [36, 44] have shown that in strongly disordered oxide glasses  $\kappa_p \ll \kappa_c$ .

### Vibrational and thermal properties from fMLPs

In general,  $\kappa(T)$  is highly sensitive to both harmonic and anharmonic vibrational properties [10, 35, 37, 45–50]; therefore, the accuracy of fMLPs in describing these properties can be quantified by comparing their predictions for  $\kappa(T)$  with those obtained from reference first principles data. To accomplish this goal, we begin by calculating the harmonic and third-order anharmonic force constants that determine the solid's vibrational energy (Eq. (1)). We do this by using either: (i) Density-Functional Theory (DFT) with the Perdew, Burke, and Ernzerhof (PBE) functional (see Refs. [30, 31] for details); or (ii) SOTA non-proprietary mp-fMLPs trained on DFT-PBE. Then, we employ these force constants to determine harmonic vibrational properties (frequencies, velocity operators, and isotopic linewidths, see Eq. (2) and Eq. (4)) and anharmonic linewidths (Eq. (3)). Subsequently, these atomistic vibrational properties are used in Eq. (5) to calculate the thermal conductivity of the 103 diverse compounds in the phononDB-PBE database. The database contains rocksalt, zincblende, and wurtzite binary compounds and involves 34 chemical species, including alkali metals (Cs, K, Li, Na, Rb), alkaline earth metals (Be, Mg, Ca, Sr, Ba), transition metals (Ag, Cu, Zn, Cd), post-transition metals (Al, Ga, In, Pb), metal-

loids (As, Sb, Si, Te, B), nonmetals (H, C, N, O, P, S, Se), and halogens (F, Cl, Br, I). Computational details are provided in the Methods.

In Fig. 1 we compare the thermal conductivity predicted from first principles (DFT-PBE) or from the mp-fMLP MACE-MP-0 (trained on DFT-PBE data) [20]. We highlight how predictions from DFT-PBE or MACE-MP-0 are generally consistent within a factor of 2 across most materials, see inset. We note that in about 20% of the compounds studied the semiclassical particle-like BTE fails to fully describe heat transport, and it is crucial to employ the more general WTE, see Fig. 5 in the Methods. These cases generally have ultra-low conductivity ( $\kappa_{\text{TOT}} \lesssim 2 \text{ W/mK}$ ), and are characterized by having wave-like tunneling conductivity ( $\kappa_c$ , accounted for by the WTE but missing from the BTE) with magnitude comparable to the particle-like propagation conductivity ( $\kappa_p$ , accounted for by both the WTE and BTE).

To understand the microscopic origin of the discrepancies in the macroscopic DFT-PBE and MACE-MP-0 conductivities, we select three representative materials — wurtzite BeO, zincblende BeTe, and rocksalt RbH — and show in Fig. 2 their phonon band structures, specific heat at constant volume, and the macroscopic thermal

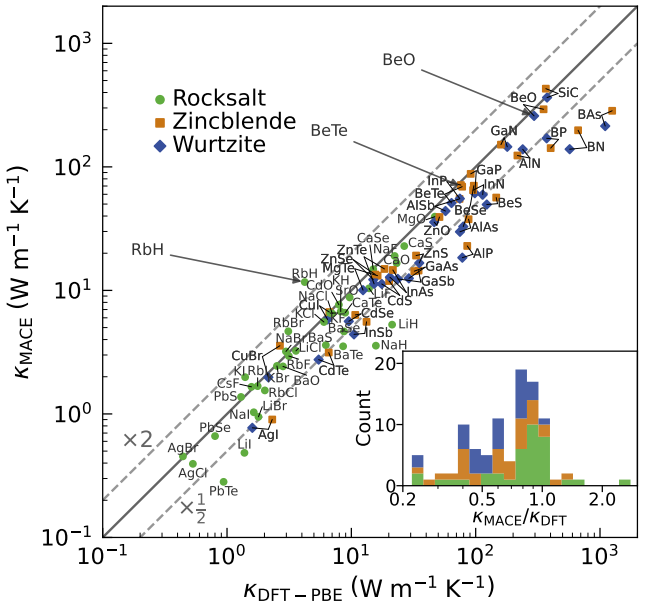


FIG. 1. **Thermal conductivity computed at 300 K from DFT-PBE or MACE-MP-0**, for 103 binary compounds taken from the phononDB-PBE database, which have rocksalt (green), zincblende (orange), and wurtzite (blue) structure. Solid lines indicate perfect agreement, while dashed lines represent discrepancies of up to a factor of 2. The arrows highlight three selected materials, which will be analyzed in detail in terms of their microscopic vibrational properties later in the manuscript. The inset displays the distribution of relative deviations between the conductivities predicted by DFT-PBE and MACE-MP-0.

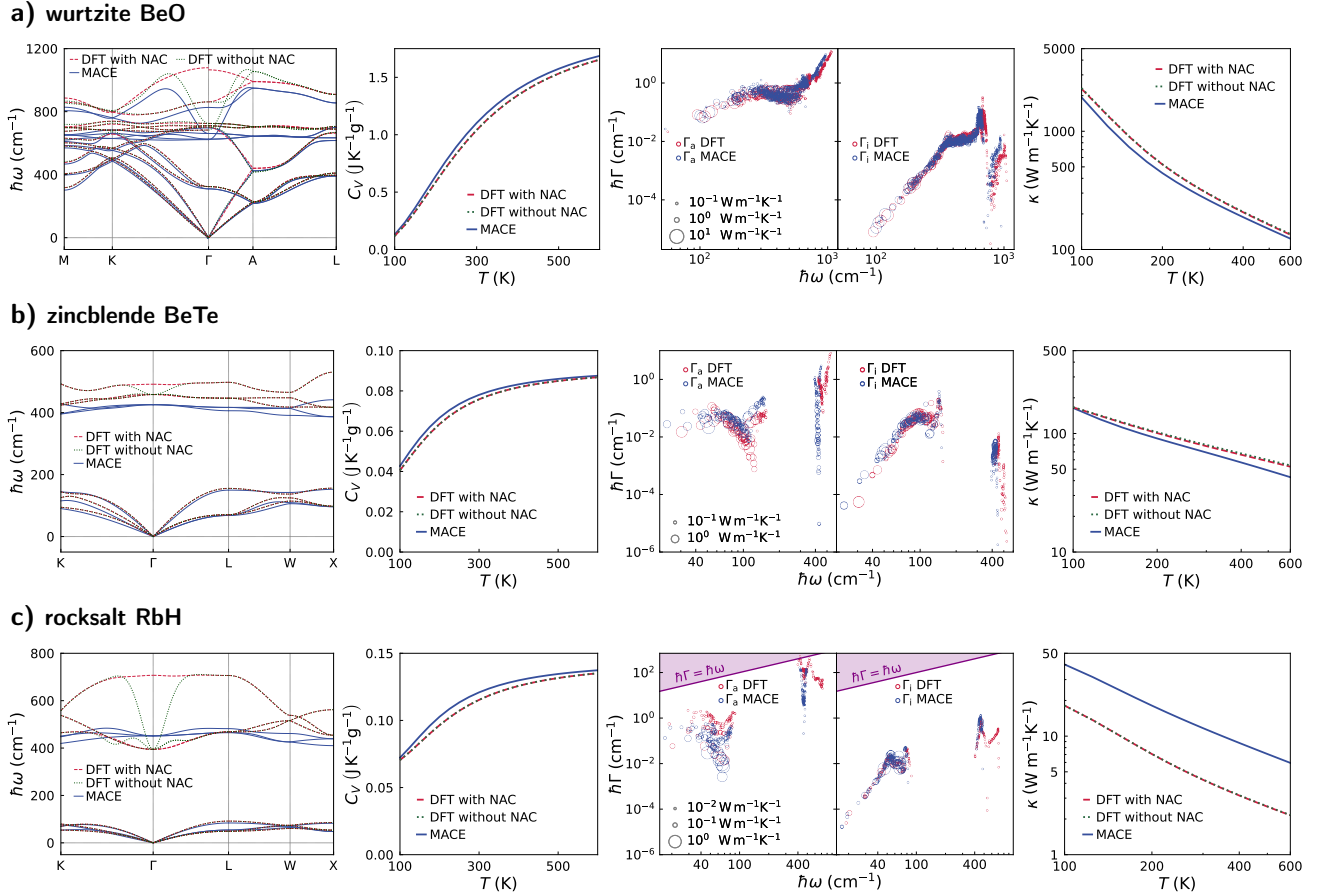


FIG. 2. **Phonon bands, specific heat at constant volume, phonon frequency-linewidth distributions, and macroscopic thermal conductivity**, for wurtzite BeO (panel a), zincblende BeTe (panel b), and rocksalt RbH (panel c). DFT-PBE values are computed using the data from Refs. [30, 31], while ‘MACE’ values are computed using the MACE-MP-0 fMLP[20]. For the DFT-PBE calculations, phonons are plotted considering the long-range non-analytical correction term (NAC, red lines or scatter points) or not (dotted green); MACE-MP-0 does not account for long-range contributions to the vibrational energy (see text). In the frequency-linewidths distributions at 300 K, we resolve the anharmonic ( $\Gamma_a$ ) and isotopic ( $\Gamma_i$ ) part of the linewidths; the areas of the markers are proportional to the contribution of the given phonon mode to the conductivity (see Eq. (6)). Specific heat and thermal conductivity are negligibly affected by considering or not the long-range NAC term.

conductivity resolved in terms of contributions from microscopic phonon modes. Examining the phonon band structures in the first column, we observe that MACE-MP-0 tends to underestimate the high-frequency optical vibrational modes compared to DFT-PBE. To further investigate these differences, we plot the DFT-PBE phonons considering the non-analytical correction term [51] (NAC, red lines or scatter points), or not (dotted green line). This long-range interaction is responsible for the energy splitting between the longitudinal-optical and transversal-optical modes in polar dielectric materials [51], and is not fully considered in fMLPs trained using a radial force cutoff (e.g., for MACE-MP-0 such cutoff is 6 Å, while it is 5 Å for SevenNet[21], CHGNet[19], and M3GNet[18]). This explains why the DFT-PBE phonons without NAC are in closer agreement with the MACE-MP-0 phonons (blue lines or scatter points). Importantly, it is noticeable that even without NAC, DFT-PBE frequencies tend to be higher than MACE-MP-0

frequencies, confirming the general tendency of MACE-MP-0 to underestimate vibrational frequencies discussed in Ref. [27]. Nevertheless, Fig. 2 shows that considering or not the NAC term has a negligible impact on the specific heat at constant volume and on the temperature-dependent conductivity ( $\kappa(T)$ ) of BeO, BeTe and RbH. This can be understood from the third column of Fig. 2, where we show that thermal transport in these materials is dominated by low-energy (acoustic) phonons, and these are negligibly affected by NAC. Specifically, these plots report the frequency-linewidth distributions, resolving both the anharmonic and isotopic contributions to the linewidths (Eq. 3 and Eq. 4, respectively), and also quantifying how much a single phonon mode contributes

to the total conductivity with the following expression:

$$\begin{aligned} \mathcal{K}(\mathbf{q})_s &= C(\mathbf{q})_s \frac{\|\mathbf{v}(\mathbf{q})_{s,s}\|^2}{3} [\Gamma(\mathbf{q})_s]^{-1} \\ &+ \sum_{s' \neq s} \frac{C(\mathbf{q})_s}{C(\mathbf{q})_s + C(\mathbf{q})_{s'}} \frac{\omega(\mathbf{q})_s + \omega(\mathbf{q})_{s'}}{2} \left[ \frac{C(\mathbf{q})_s}{\omega(\mathbf{q})_s} + \frac{C(\mathbf{q})_{s'}}{\omega(\mathbf{q})_{s'}} \right] \\ &\times \frac{\|\mathbf{v}(\mathbf{q})_{s,s'}\|^2}{3} \frac{\frac{1}{2} [\Gamma(\mathbf{q})_s + \Gamma(\mathbf{q})_{s'}]}{[\omega(\mathbf{q})_{s'} - \omega(\mathbf{q})_s]^2 + \frac{1}{4} [\Gamma(\mathbf{q})_s + \Gamma(\mathbf{q})_{s'}]^2}. \end{aligned} \quad (6)$$

This equation describes how much a single phonon mode  $(\mathbf{q})_s$  contributes to heat conduction. Specifically, the term on the first line accounts for the aforementioned particle-like conduction mechanism; the term on the second and third lines, instead, describes the wave-like conduction that originates from tunneling between two non-degenerate phonons  $(\mathbf{q})_s$  and  $(\mathbf{q})_{s'}$  — here the single-phonon contributions from  $(\mathbf{q})_s$  is resolved using the ratio between specific heats  $\frac{C(\mathbf{q})_s}{C(\mathbf{q})_s + C(\mathbf{q})_{s'}}$  as weight, as discussed by Eq. (E3) in [35].

The frequency-linewidth distributions in Fig. 2a show overall agreement between DFT-PBE and MACE-MP-0 for the phonon modes that are mainly contributing to conduction — the acoustic modes and the optical modes with  $\hbar\omega(\mathbf{q})_s < k_B T$  — and we see that this implies very similar values for the corresponding macroscopic  $\kappa(T)$  (with a relative difference  $< 10\%$ ). Importantly, Fig. 2b shows compatibility between  $\kappa(T)$  predicted from DFT-PBE or MACE-MP-0 can also result from cancellation of errors; specifically, in BeTe there are visible differences in the frequency-linewidth distributions, and these largely cancel out when integrated to determine the conductivity. Finally, Fig. 2c illustrates that the presence of systematic, non-compensating differences in the microscopic frequency-linewidth distributions can also directly translate into significant discrepancies on the macroscopic conductivities (difference of a factor of 2.7). Additionally, we note that depending on the the chemical composition, the anharmonic linewidths at room temperature can either dominate over the isotopic linewidth (e.g., in BeO) or not (e.g., in BeTe). In the former case, the thermal conductivity is practically unaffected by considering or not the isotopic contributions to the linewidth, while in the latter case considering isotopic scattering yields a reduction of  $\kappa(300\text{ K})$  of about  $\sim 75\%$  (see Table. II).

The results above motivate us to investigate when good agreement between DFT and fMLP conductivities is obtained from accurately described microscopic harmonic and anharmonic vibrational properties, or because of compensation of errors. To achieve this goal, we resolve the discrepancies in the total macroscopic thermal conductivities using the Symmetric Relative Error (SRE),

$$\text{SRE}[\kappa] = 2 \frac{|\kappa_{\text{fMLP}} - \kappa_{\text{DFT}}|}{\kappa_{\text{fMLP}} + \kappa_{\text{DFT}}}. \quad (7)$$

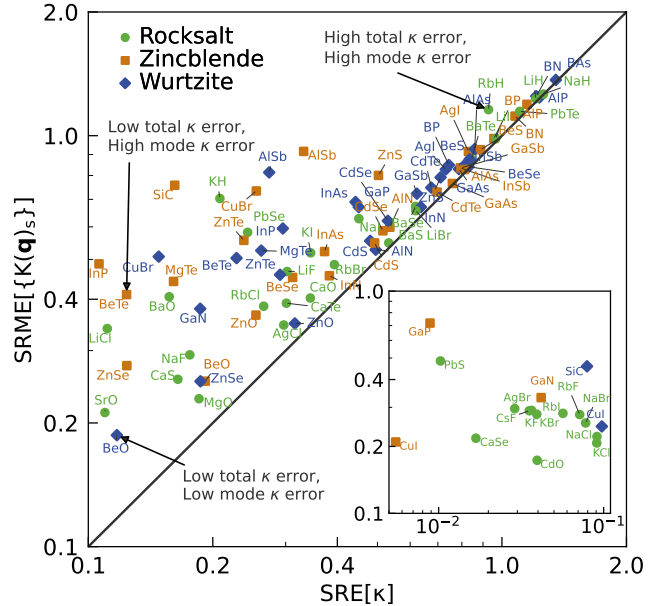


FIG. 3. **Errors on conductivity: SRE & SRME**, computed comparing DFT-PBE and fMLP (MACE-MP-0) predictions in 103 chemically and structurally diverse compounds. Large discrepancies between DFT-PBE and fMLP on microscopic, single-phonon conductivity contributions are described by large SRME (Eq. (8)), which implies a significant discrepancy between the macroscopic DFT-PBE and fMLP conductivities, and thus large SRE (Eq. (7)). Three materials are highlighted: wurtzite BeO shows low SRME and thus low SRE; rocksalt RbH displays high error in both SRME and SRE; zincblende BeTe exhibits high SRME but low SRE because of compensation of microscopic errors.

Then, to determine whether a low value for  $\text{SRE}[\kappa]$  originates from accurately described microscopic vibrational properties, or because of compensation of errors, we introduce the Symmetric Relative Mean Error (SRME) on the single-phonon conductivity contribution  $\mathcal{K}(\mathbf{q})_s$ :

$$\text{SRME}[\{\mathcal{K}(\mathbf{q})_s\}] = \frac{2}{N_c \mathcal{V}} \frac{\sum_{\mathbf{q}s} |\mathcal{K}_{\text{fMLP}}(\mathbf{q})_s - \mathcal{K}_{\text{DFT}}(\mathbf{q})_s|}{\mathcal{K}_{\text{fMLP}} + \mathcal{K}_{\text{DFT}}}, \quad (8)$$

where  $\mathcal{K}_{\text{DFT}}(\mathbf{q})_s$  refers to Eq. (8) evaluated using DFT, and  $\mathcal{K}_{\text{fMLP}}(\mathbf{q})_s$  refers to the same equation evaluated using fMLP. Fig. 3 illustrates that a large SRME generally implies large SRE. Importantly, knowing both SRE and SRME enables us to identify when microscopic error compensation occurs — this is indicated by a large SRME but small SRE. Three representative cases are highlighted in Fig. 3: wurtzite BeO shows low SRME and thus correspondingly low SRE; rocksalt RbH exhibits high error in both SRME and SRE; zincblende BeTe displays high SRME but low SRE due to compensation of microscopic errors. We note that the  $\text{SRME}[\mathcal{K}(\mathbf{q})_s]$  error can stem from discrepancies in the harmonic (second-order) or anharmonic (third-order) force constants. Therefore, in Fig. 6 in the Methods we discuss how to disentangle

the SRME and SRE into errors on harmonic vibrational properties and anharmonic vibrational properties.

Overall, this analysis highlights the importance of benchmarking the accuracy of fMLPs not only at the macroscopic but also at the microscopic level. In particular the macroscopic SRE[ $\kappa$ ] alone is not a reliable descriptor for the fMLPs' ability to capture the harmonic and anharmonic physics underlying heat conduction. However, achieving both a small macroscopic SRE[ $\kappa$ ] and a small microscopic SRME[ $\kappa$ ] is a sufficient condition for accurately describing both the microscopic physics and the macroscopic thermal conductivity.

### Accuracy of various SOTA foundation models

The previous section demonstrated that the SRE and SRME descriptors can effectively measure the accuracy of fMLPs in describing vibrational and thermal properties. Therefore, here we utilize these descriptors to compare the accuracy of different non-proprietary mp-fMLPs on the 103 diverse structures contained in the phononDB-PBE database[30, 31]. Fig. 4 compares the accuracy of the four foundation models M3GNet[18], CHGNet[19], MACE-MP-0[20], and SevenNet[21] mp-fMLPs. To determine if a certain mp-fMLP tends to systematically overestimate or underestimate the conductivity, it is useful to rely on the Symmetric Relative Difference (SRD) in the total Wigner conductivity from DFT-PBE or mp-fMLP,

$$\text{SRD}[\kappa] = 2 \frac{\kappa^{\text{fMLP}} - \kappa^{\text{DFT}}}{\kappa^{\text{fMLP}} + \kappa^{\text{DFT}}}, \quad (9)$$

which ranges from -2 to +2, resolving both overestimation and underestimation of the conductivity. Figure 4a summarizes the SRD for all 103 binary compounds in the phononDB-PBE database, as depicted in the violin plot [52]. In this plot, the width of each violin shape is related to the percentage of materials with SRD values indicated on the y-axis. The median SRD value is marked by a white scatter point, while the black boxes illustrate the interquartile range, and the whiskers show 1.5 times the interquartile range below and above the first and third quartile points. Unstable structures with negative phonon frequencies were included considering  $\kappa^{\text{fMLP}} = 0$ , *i.e.*, SRD = -2. This analysis reveals that all the mp-fMLPs assessed in this study tend to underestimate the thermal conductivity. This finding is consistent with the observed systematic underestimation of vibrational frequencies noted in Ref. [27], and might also be derived from overestimation of anharmonic linewidths.

To examine whether the SRD shown in Fig. 4a is influenced by error compensation, we analyze in Fig. 4b the violin plots for SRME[ $\{\mathcal{K}(\mathbf{q})_s\}$ ]. We see that the SRME distribution for MACE-MP-0 is the closest to zero, followed by SevenNet, M3GNet, and CHGNet. In addition, to quantify the overall accuracy of a fMLPs in predicting the macroscopic conductivity over a materials' database,

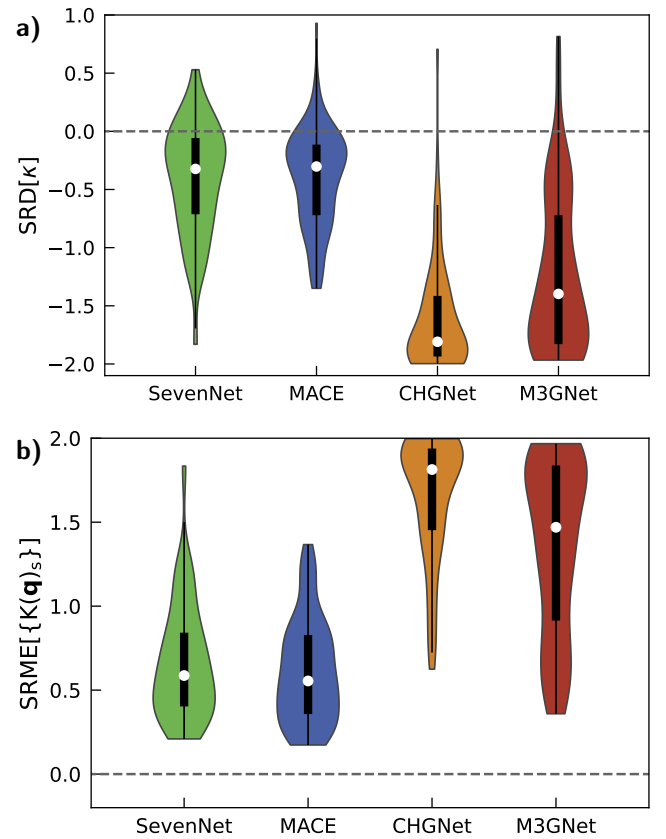


FIG. 4. **Performance of mp-fMLPs in calculating thermal conductivity.** Panel a presents violin plots depicting the Symmetric Relative Difference (SRD) in the total Wigner thermal conductivity (Eq. (9)) for mp-fMLPs SevenNet[21], MACE-MP-0[20], CHGNet[19], M3GNet[18]. Panel b shows the SRME for mode-resolved thermal conductivity. In both panels, the medians are marked with white scatter points, the widths of the boxes represent the interquartile range, and the whiskers show the range of data points without outliers.

without resolving the possible compensation of microscopic errors, it is informative to consider the mean of the modulus of the deviations, *i.e.*, the mean of the distribution of SRE (7) — we prefer this over the mean of the SRD distribution, as the latter can be close to zero in the presence of very broad but symmetric distribution. Importantly, we note that the mean for SRE[ $\kappa$ ] and mean for SRME[ $\mathcal{K}(\mathbf{q})_s$ ] are expected to be comparable in the absence of compensation of microscopic errors. In contrast, in the presence of compensation of microscopic errors, the mean SRE[ $\kappa$ ] is significantly lower than mean SRME[ $\mathcal{K}(\mathbf{q})_s$ ]. The mean values for SRME[ $\mathcal{K}(\mathbf{q})_s$ ] and SRE[ $\kappa$ ] are reported in Table I.

In summary, our findings reveal that the mean SRE[ $\kappa$ ] and the mean in SRME[ $\mathcal{K}(\mathbf{q})_s$ ] are effective metrics for assessing the accuracy of mp-fMLPs in predicting macroscopic thermal conductivity. These metrics not only indicate the precision in predicting the macroscopic conductivity (low SRE[ $\kappa$ ]), but can also assess whether

	SevenNet	MACE	CHGNet	M3GNet
Mean in SRE[ $\kappa$ ]	0.597	0.512	1.695	1.397
Mean in SRME[ $\{\mathcal{K}(\mathbf{q})_s\}$ ]	0.767	0.664	1.717	1.469

TABLE I. **Mean of SRE[ $\kappa$ ] and SRME[ $\{\mathcal{K}(\mathbf{q})_s\}$ ]** for different mp-fMLPs. Different (similar) values for SRE[ $\kappa$ ] and SRME[ $\{\mathcal{K}(\mathbf{q})_s\}$ ] indicate presence (absence) of compensation of microscopic errors. Smaller values for SRME[ $\{\mathcal{K}(\mathbf{q})_s\}$ ] correspond to higher accuracy in predicting both microscopic vibrational properties, and macroscopic thermal conductivity.

accurate conductivity predictions follow from accurate estimates of microscopic vibrational and thermal properties (low SRE[ $\kappa$ ] and low SRME[ $\{\mathcal{K}(\mathbf{q})_s\}$ ]) or result from compensation of microscopic errors (low SRE[ $\kappa$ ] and large SRME[ $\{\mathcal{K}(\mathbf{q})_s\}$ ]).

## Discussion

We have introduced a robust and automated computational framework for directly predicting the thermal conductivity of solids using foundation Machine Learning Potentials. This framework has been employed to benchmark the out-of-the-box accuracy of SOTA fMLPs trained on the Materials Project DFT-PBE database [38] (mp-fMLPs) — SevenNet[21], MACE-MP-0[20], CHGNet[19], and M3GNet[18] — in predicting both microscopic harmonic and anharmonic vibrational properties, and the macroscopic thermal conductivity. In particular, we compared predictions from mp-fMLP against those obtained from the first-principles phononDB-PBE database, which includes 103 diverse compounds, made up of 34 different chemical species and having wurtzite, zincblende, or rocksalt structure [30, 31]. Our results show that the overall most accurate mp-fMLPs, MACE-MP-0[20], yields conductivities compatible within a factor of two of the DFT-PBE values for 69% of the materials in the phononDB-PBE database[30, 31]. We have shown that non-proprietary SOTA mp-fMLPs yield thermal conductivity predictions that tend to underestimate the corresponding first-principles DFT-PBE values, quantifying these discrepancies with the parameter SRD[ $\kappa$ ]. Most importantly, we have introduced a descriptor quantifies the performance of mp-fMLPs in predicting both microscopic harmonic and anharmonic vibrational properties, and the macroscopic, experimentally measurable thermal conductivity — the Symmetric Relative Mean Error on the conductivity SRME[ $\{\mathcal{K}(\mathbf{q})_s\}$ ]. This descriptor provides a metric that could be useful to training or fine-tune fMLPs, and its mean computed over a database of materials can be used to benchmark the accuracy of different families of mp-fMLPs. We have also provided computational recipes for incorporating the Mean in SRME[ $\{\mathcal{K}(\mathbf{q})_s\}$ ] into standard benchmark

frameworks used to assess the accuracy of fMLPs [25]. Finally, we have discussed how our automated framework to compute the Wigner conductivity can accurately describe materials that violate semiclassical Boltzmann transport. These often feature very low conductivity ( $\lesssim 2$  W/mK) and are potentially relevant for e.g., heat-shielding [10] and thermoelectric [9] technologies. Ultimately, the computational framework and analyses that we presented pave the way for quantum-accurate, physics-aware predictions of thermal conductivity of materials with arbitrary composition and structure.

## Methods

**Failures of semiclassical Boltzmann transport in binary crystals with low conductivity.** Our automated framework can be used to identify materials in which the semiclassical BTE fails. In particular, the BTE [39] describes heat propagation exclusively in terms of particle-like phonons that propagate and scatter akin to the particles of a classical gas. While the BTE is accurate in weakly anharmonic and ordered ‘simple crystal’ (characterized by phonon interband spacings much larger than the linewidths[34, 41]), it fails in strongly anharmonic or disordered materials (with phonon interband spacings smaller than the linewidths). It has been recently shown [10, 34, 35, 45, 48] that in the latter cases heat conduction originates not only from particle-like propagation but also from wave-like interband tunneling of phonons. The recently developed WTE generalizes the BTE by accounting for both particle-like propagation and wave-like tunneling contributions to the conductivity ( $\kappa_P$  and  $\kappa_C$ , respectively; the total conductivity is given by  $\kappa_{TOT} = \kappa_P + \kappa_C$ ), providing a comprehensive approach that overcomes the failures of the BTE.

Our automated framework computes the Wigner thermal conductivity[35], and therefore can be used to find materials that have very low thermal conductivity, relevant for thermoelectric or heat-shielding technologies. In Fig. 5 we show that among the 103 compounds analyzed, the BTE fails in materials with low thermal conductivity ( $\kappa_{TOT} \lesssim 2$  W/mK), such as AgBr and AgCl, since the wave-like tunneling conductivity becomes comparable to the particle-like propagation conductivity. We also note that in simple crystals with large conductivity, the BTE is accurate as the population conductivity dominates over the wave-like tunneling conductivity.

**Symmetric Relative Mean Error on harmonic and anharmonic vibrational properties.** The analyses reported in the main text discusses SRME[ $\{\mathcal{K}(\mathbf{q})_s\}$ ] as a descriptor that is informative of the accuracy of fMLPs in describing microscopic harmonic and anharmonic properties. In this section we provide the tools to resolve whether the SRME[ $\{\mathcal{K}(\mathbf{q})_s\}$ ] originates from errors in microscopic harmonic properties, anharmonic

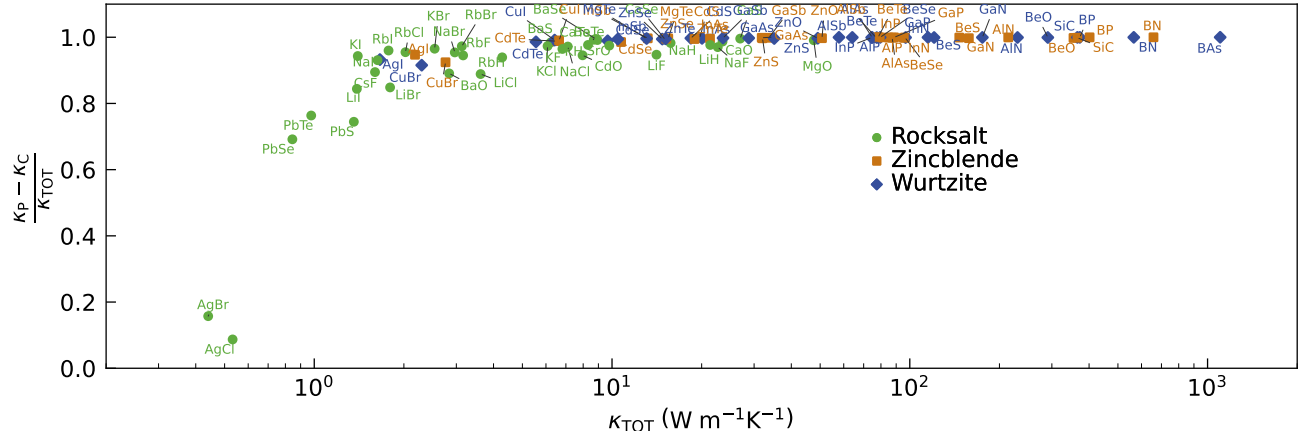


FIG. 5. **Failures of semiclassical Boltzmann transport in binary crystals with low conductivity** and having rocksalt (green), zincblende (orange), and wurtzite (blue) structure. These occur when the conductivity described by the BTE in terms of particle-like propagation of phonons ( $\kappa_P$ ) does not dominate over the coherences conductivity determined by wave-like tunneling of phonons ( $\kappa_C$ ). The WTE [35] accounts for both  $\kappa_P$  and  $\kappa_C$ , and failures from semiclassical Boltzmann transport are highlighted by a relative strength of particle-wave transport  $(\kappa_P - \kappa_C)/(\kappa_P + \kappa_C)$  appreciably smaller than one. These conductivities were obtained from the DFT-PBE force constants in the phononDB-PBE dataset.

properties, or both. To this aim, we employ the expression for the microscopic, single-phonon contributions to the thermal conductivity (6) to define descriptors that quantify the accuracy with which harmonic and anharmonic properties are predicted. In particular, we note that the conductivity contribution of a phonon  $(\mathbf{q})_s$  is a function of: (i) all the phonon frequencies  $\{\omega(\mathbf{q})_{s'}\}$  at a fixed wavevector  $\mathbf{q}$  and variable mode  $s' = 1, \dots, N_s$  ( $N_s$  is the number of phonon bands, equal to 3 times the number of atoms in the crystal's unit cell [53]); (ii) all velocity-operator elements  $\{\mathbf{v}(\mathbf{q})_{s,s'}\}$  at fixed  $\mathbf{q}$ ,  $s$  and variable  $s'$ ; (iii) all isotopic

linewidths at fixed  $\mathbf{q}$  and variable  $s'$ ,  $\{\Gamma_i(\mathbf{q})_{s'}\}$ , which depend solely on harmonic properties, see Eq. 4; (iv) the anharmonic linewidths  $\{\Gamma_a(\mathbf{q})_{s'}\}$  at fixed  $\mathbf{q}$  and variable  $s'$ . This can be summarized using the following notation:  $\mathcal{K}(\mathbf{q})_s = \mathcal{K}(\mathbf{q})_s[\{\omega(\mathbf{q})_{s'}\}, \{\mathbf{v}(\mathbf{q})_{s,s'}\}, \{\Gamma_i(\mathbf{q})_{s'}\}, \{\Gamma_a(\mathbf{q})_{s'}\}]$  where the curly brackets denote the set of values of a certain quantity over all the bands at fixed  $\mathbf{q}$  (e.g.,  $\{\omega(\mathbf{q})_{s'}\} = \{\omega(\mathbf{q})_1, \omega(\mathbf{q})_2, \dots, \omega(\mathbf{q})_{N_s}\}$ ).

To quantify the impact of errors on the harmonic (har) and anharmonic (anh) properties on the single-phonon conductivity contributions, we define the Symmetric Relative Mean Error (SRME) on these properties as follows:

$$\text{SRME[har]} = 2 \frac{\sum_{qs} |\mathcal{K}(\mathbf{q})_s[\{\omega_{\text{fMLP}}(\mathbf{q})_{s'}\}, \{\mathbf{v}_{\text{fMLP}}(\mathbf{q})_{s,s'}\}, \{\Gamma_{i,\text{fMLP}}(\mathbf{q})_{s'}\}, \{\Gamma_{a,\text{DFT}}(\mathbf{q})_{s'}\}] - \mathcal{K}_{\text{DFT}}(\mathbf{q})_s|}{\sum_{qs} (\mathcal{K}(\mathbf{q})_s[\{\omega_{\text{fMLP}}(\mathbf{q})_{s'}\}, \{\mathbf{v}_{\text{fMLP}}(\mathbf{q})_{s,s'}\}, \{\Gamma_{i,\text{fMLP}}(\mathbf{q})_{s'}\}, \{\Gamma_{a,\text{DFT}}(\mathbf{q})_{s'}\}] + \mathcal{K}_{\text{DFT}}(\mathbf{q})_s)}, \quad (10)$$

$$\text{SRME[anh]} = 2 \frac{\sum_{qs} |\mathcal{K}(\mathbf{q})_s[\{\omega_{\text{DFT}}(\mathbf{q})_{s'}\}, \{\mathbf{v}_{\text{DFT}}(\mathbf{q})_{s,s'}\}, \{\Gamma_{i,\text{DFT}}(\mathbf{q})_{s'}\}, \{\Gamma_{a,\text{fMLP}}(\mathbf{q})_{s'}\}] - \mathcal{K}_{\text{DFT}}(\mathbf{q})_s|}{\sum_{qs} (\mathcal{K}(\mathbf{q})_s[\{\omega_{\text{DFT}}(\mathbf{q})_{s'}\}, \{\mathbf{v}_{\text{DFT}}(\mathbf{q})_{s,s'}\}, \{\Gamma_{i,\text{DFT}}(\mathbf{q})_{s'}\}, \{\Gamma_{a,\text{fMLP}}(\mathbf{q})_{s'}\}] + \mathcal{K}_{\text{DFT}}(\mathbf{q})_s)}, \quad (11)$$

where we have used the shorthand notation  $\mathcal{K}_{\text{DFT}}(\mathbf{q})_s = \mathcal{K}_{\text{DFT}}(\mathbf{q})_s[\{\omega_{\text{DFT}}(\mathbf{q})_s\}, \{\mathbf{v}_{\text{DFT}}(\mathbf{q})_{s,s'}\}, \{\Gamma_{i,\text{DFT}}(\mathbf{q})_{s'}\}, \{\Gamma_{a,\text{DFT}}(\mathbf{q})_{s'}\}]$ . Intuitively, SRME[har] (10) is large when harmonic vibrational properties ( $\omega(\mathbf{q})_s$ , or  $\mathbf{v}(\mathbf{q})_{s,s'}$ , or  $\Gamma_i(\mathbf{q})_s$ ) differ between DFT and fMLP, while SRME[anh] (11) is large when the anharmonic linewidths ( $\Gamma_a(\mathbf{q})_s$ ) differ between DFT and fMLP. We show in Fig. 6 that small SRME[har] and small SRME[anh] (e.g., as in BeO), imply a small SRE[ $\kappa$ ] Fig. 6 also shows that often large SRME[har] and large SRME[anh] (e.g. RbH) translate into large SRE[ $\kappa$ ]; however there also cases (e.g. BeTe)

in which large SRME[har] and large SRME[anh] can also compensate each other and result in a small SRE[ $\kappa$ ]. This confirms the statements made in the main text on SRE[ $\kappa$ ] not being a reliable descriptor for the capability of fMLPs to capture the harmonic and anharmonic physics underlying heat conduction. In contrast, having both small SRME[har] and small SRME[anh] is a sufficient condition to accurately capture harmonic and anharmonic vibrational properties, as well as thermal conductivity.

Overall, these tests highlight the importance of

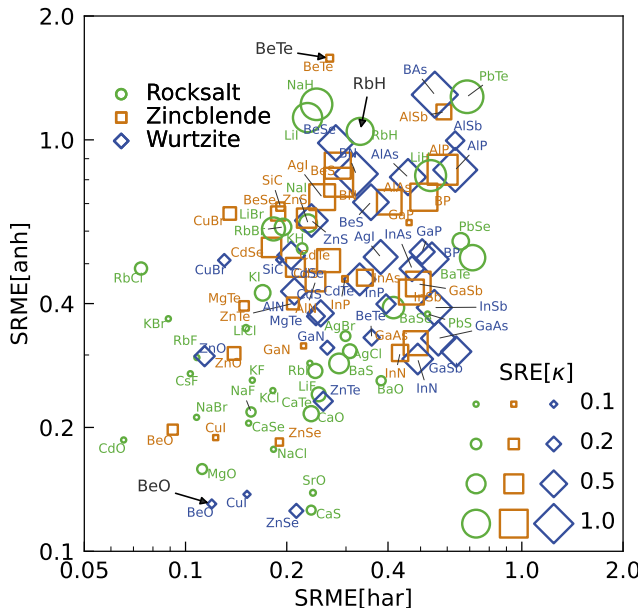


FIG. 6. **Relation between harmonic and anharmonic errors, and thermal conductivity**, calculated for 103 compounds using Eq. (10) and Eq. (11) considering DFT and MACE-MP-0[20]. The area of the marker is proportional to the symmetric percentage error in the average total conductivity (SRE[ $\kappa$ ], see legend). We highlight how BeO (RbH) has low (large) SRME[har], SRME[anh], and SRE[ $\kappa$ ]; in contrast, BeTe displays large SRME[har], SRME[anh], but low SRE[ $\kappa$ ] due to compensation of errors (see text).

benchmarking for the accuracy of fMLPs in predicting both microscopic harmonic and anharmonic vibrational properties, motivating the introduction of the SRME[ $\{\mathcal{K}(\mathbf{q})_s\}$ ].

### Influence of isotopic scattering on conductivity.

To analyze the influence of isotope scattering on the conductivity, we compare thermal conductivity values with and without considering the linewidths from isotope mass-disorder, as described in Eq. (4). The results are summarized in Table II. In wurtzite BeO and rocksalt RbH, the impact of isotope scattering is minimal or small, respectively. However, in zincblende BeTe, as shown in Fig. 2b, isotopic and anharmonic linewidths have comparable values, both affecting the

	wurtzite BeO		zincblende BeTe		rocksalt RbH	
	DFT	MACE	DFT	MACE	DFT	MACE
with $\Gamma_i(\mathbf{q})_s$	286.391	259.443	78.246	69.138	4.281	11.682
without $\Gamma_i(\mathbf{q})_s$	291.963	263.956	289.374	402.030	4.682	14.672

TABLE II. **Influence of isotopic scattering on the thermal conductivity at 300 K** for BeO, BeTe, and RbH.

thermal conductivity. In this material, MACE-MP-0 significantly overestimates some linewidths compared to DFT-PBE, and this compensates for the overestimation in other regions. Consequently, MACE-MP-0 shows a significantly larger error in thermal conductivity when isotope scattering is not considered.

**Automated Wigner Conductivity Workflow.** The workflow, outlined in Fig. 7, includes structure relaxation, force constant computation, and thermal conductivity analysis. To automate the calculation of interatomic forces, we developed an interface between the `ase`[54] (version 3.23.0) and the `phonopy`[30, 55] (version 3.2.0) packages. Atomic positions and cell parameters were simultaneously relaxed to minimize stresses and ensure positive phonon frequencies. Since the determination of irreducible  $\mathbf{q}$  points during thermal conductivity calculations depends on the crystal symmetry, it is essential to consider symmetries. During the initial relaxation stage, symmetries are explicitly enforced as constraints while simultaneously relaxing atomic positions and cell parameters. After each step of atomic position relaxation, cell parameters are adjusted if the total forces exceed a certain threshold (values are fMLP-specific and discussed later). In the second stage, the symmetry constraint is removed to allow for finer atomic adjustments and a complete relaxation of the structure. The joint relaxation of atomic positions and cell parameters is applied once more. If the symmetry is preserved, the final relaxed structure is used. If symmetry is broken, the structure from the first stage, with enforced symmetry, is retained. Finally, an additional relaxation of atomic positions with fixed cell parameters is performed using a stricter threshold to ensure the structure reaches a stable energy minimum at a fixed volume for accurate phonon calculations.

To ensure positive phonons, strict thresholds were established, tailored to the performance of each individual model. M3GNet required thresholds of  $2.0 \times 10^{-3}$  eV/Å and  $8.0 \times 10^{-4}$  eV/Å. For CHGNet, MACE-MP-0, and SevenNet, the thresholds were set to  $10^{-4}$  eV/Å and  $5.0 \times 10^{-5}$  eV/Å for initial and final values, respectively. In the supercell force-constant calculations, we used the same parameters used in the DFT reference data[30, 31].

Thermal conductivities were computed using `phonopy` following Ref. [30, 55]. A  $19 \times 19 \times 19$   $q$ -mesh was used for rocksalt and zincblende structures, and a  $19 \times 19 \times 15$   $q$ -mesh for wurtzite structures, with collision operator computed using the tetrahedron method. For Fig. 2, anharmonic linewidths were calculated on a  $9 \times 9 \times 9$   $q$ -mesh to ensure clarity. We utilized version 3 of `phonopy` for anharmonic linewidth calculations and employed the Wang method [56, 57] for the NAC term, as implemented in the `phonopy`[55, 58] package (version 2.26.6). When structures with negative phonon frequencies were found with mp-fMLPs, these

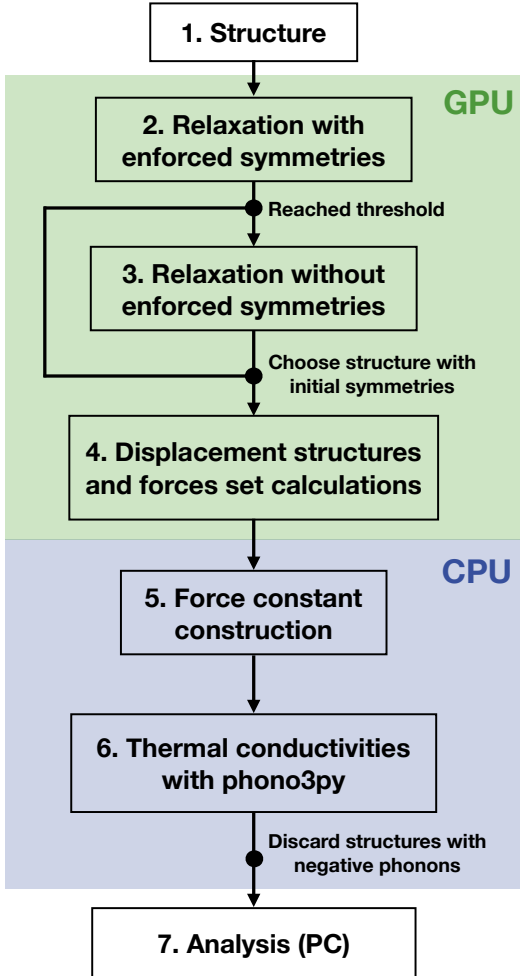


**FIG. 7. Automated Wigner Conductivity Workflow.** The first part of the workflow, involving force evaluation, is performed on a GPU. The input structures undergo relaxation in two stages. In the first stage, initial symmetries are enforced while simultaneously relaxing atomic positions and cell parameters. In the second stage, the structure is further relaxed by removing the symmetry constraint. If the symmetry group of the final structure changes, the structure with enforced symmetry relaxation is used instead. After initializing the displacement structures, the force sets are calculated for each displacement. CPUs handle the remainder of the workflow. Force constants are constructed from the displacement force sets, and thermal conductivity is calculated using `phonopy3py`. Structures with negative phonon frequencies are discarded from the final analysis (conducted on a PC).

were discarded from subsequent thermal-conductivity analysis.

**DFT and mp-fMLP calculations.** Structures were taken from the Materials Project (MP)[38]. The Perdew, Burke, and Ernzerhof (PBE) exchange-correlation functional [59] was employed for DFT calculations, consistent with the approach used for generating MP dataset. The computational details for the DFT calculations can be

found in Refs. [30, 31]. As discussed in Refs. [18–21], mp-fMLP were trained on the MP data using the PBE functional. M3GNet was used through the `matgl`[60] (version 1.1.2) package with the M3GNet-MP-2021.2.8-PES model. The CHGNet version 0.3.8 was used. The MACE-MP-0 2024-01-07-mace-128-L2 model was run through LAMMPS[61]. SevenNet was used through the `seven` package (version 0.9.2) with the SevenNet-0\_11July2024 model.

**Computational cost.** The SevenNet, MACE, and CHGNet calculations were performed on an Nvidia Tesla A100 SXM4 80GB GPU, with the relaxation and force calculations for all 103 structures costing approximately  $\sim 3$  GPU hours per model. M3GNet was executed on AMD EPYC 7702 CPUs, with relaxation and force calculations costing around  $\sim 30$  CPU hours. Thermal conductivity calculations for all 103 structures required about  $\sim 50$  CPU hours per model, and similar resources were needed for evaluating thermal conductivity from the DFT force constants. Overall, the analysis of these four models required approximately  $\sim 9$  GPU hours and  $\sim 280$  CPU hours.

**Data availability.** The phononDB-PBE dataset including the displacements generated by `phonopy3py` and the corresponding force sets are available <https://github.com/atztogo/phonondb> [30, 31]. The remaining dataset will be made available in the future.

**Code availability.** The `phonopy3py` and `phonopy` packages are available at <https://github.com/phonopy/>; the `ase` package is available at <https://gitlab.com/ase/ase>. `matgl` containing the M3GNet model is available at <https://github.com/materialsvirtuallab/matgl>; the CHGNet model and package is available at <https://github.com/CederGroupHub/chgnet>; the SevenNet model and package is available at <https://github.com/MDIL-SNU/SevenNet>. The MACE used through LAMMPS[61] is available at <https://github.com/ACESuit/lammps>, and the MACE-MP-0 model is available at <https://github.com/ACESuit/mace-mp>. The automatic framework and the analysis code will be made available soon.

**Competing interests.** The authors declare no competing interests.

**Author contributions.** M.S. conceived and supervised the project. B.P. developed the automated computational framework and performed the numerical calculations with inputs from P.A., G.C., and M.S. B.P. and M.S. analyzed and organized the data, with inputs from

P.A. All authors contributed to discussing the data, writing and editing the manuscript.

## ACKNOWLEDGEMENTS

M. S. acknowledges support from: (i) Gonville and Caius College; (ii) the Swiss National Science Foundation (SNSF) project P500PT\_203178; (iii) the Sulis Tier 2 HPC platform (funded by EPSRC Grant EP/T022108/1 and the HPC Midlands+consortium); (iv) the Kelvin2 HPC platform at the NI-HPC Centre (funded by EPSRC and jointly managed by Queen's University Belfast and Ulster University). P.A. acknowledges support from SNSF through Post.Doc mobility fellowship P500PN\_206693. We thank William Chuck Witt for the useful discussions, and we gratefully acknowledge Atsushi Togo for having provided harmonic and anharmonic force constants computed using density functional theory (PBE functional) from the phononDB-PBE database [30, 31].

---

\* [ms2855@cam.ac.uk](mailto:ms2855@cam.ac.uk)

- [1] T. B. Blank, S. D. Brown, A. W. Calhoun, and D. J. Doren, *The Journal of Chemical Physics* **103**, 4129 (1995).
- [2] A. P. Bartók, M. C. Payne, R. Kondor, and G. Csányi, *Physical Review Letters* **104**, 136403 (2010).
- [3] R. Drautz, *Physical Review B* **99**, 014104 (2019), publisher: American Physical Society.
- [4] A. Seko, A. Togo, and I. Tanaka, *Physical Review B* **99**, 214108 (2019).
- [5] E. Kocer, T. W. Ko, and J. Behler, *Annual Review of Physical Chemistry* **73**, 163 (2022).
- [6] S. Batzner, A. Musaelian, L. Sun, M. Geiger, J. P. Mailoa, M. Kornbluth, N. Molinari, T. E. Smidt, and B. Kozinsky, *Nature Communications* **13**, 2453 (2022), publisher: Nature Publishing Group.
- [7] A. Togo and A. Seko, *The Journal of Chemical Physics* **160**, 211001 (2024).
- [8] G. F. Nataf, S. Volz, J. Ordóñez-Miranda, J. Íñiguez González, R. Rurrali, and B. Dkhil, *Nature Reviews Materials* , 1 (2024).
- [9] S. A. J. Kimber, J. Zhang, C. H. Liang, G. G. Guzmán-Verri, P. B. Littlewood, Y. Cheng, D. L. Abernathy, J. M. Hudspeth, Z.-Z. Luo, M. G. Kanatzidis, T. Chatterji, A. J. Ramirez-Cuesta, and S. J. L. Billinge, *Nature Materials* **22**, 311 (2023).
- [10] A. Pazhedath, L. Bastonero, N. Marzari, and M. Simoncelli, accepted in *Phys. Rev. Applied* (2024), [arXiv:2309.10789](https://arxiv.org/abs/2309.10789) [cond-mat.mtrl-sci].
- [11] W. C. Witt, C. van der Oord, E. Gelžinytė, T. Järvinen, A. Ross, J. P. Darby, C. H. Ho, W. J. Baldwin, M. Sachs, J. Kermode, N. Bernstein, G. Csányi, and C. Ortner, *The Journal of Chemical Physics* **159**, 164101 (2023).
- [12] R. Okabe, A. Chotrattanapituk, A. Boonkird, N. Andrejevic, X. Fu, T. S. Jaakkola, Q. Song, T. Nguyen, N. Drucker, S. Mu, Y. Wang, B. Liao, Y. Cheng, and M. Li, *Nature Computational Science* [10.1038/s43588-024-00661-0](https://doi.org/10.1038/s43588-024-00661-0) (2024).
- [13] J. Ojih, M. Al-Fahdi, Y. Yao, J. Hu, and M. Hu, *Journal of Materials Chemistry A* **12**, 8502 (2024).
- [14] A. Rodriguez, C. Lin, H. Yang, M. Al-Fahdi, C. Shen, K. Choudhary, Y. Zhao, J. Hu, B. Cao, H. Zhang, *et al.*, *npj Computational Materials* **9**, 20 (2023).
- [15] V. D. Rose, A. Kozachinskiy, C. Rojas, M. Petrache, and P. Barceló, *Three iterations of \$(d-1)\$-WL test distinguish non isometric clouds of \$d\$-dimensional points* (2023), arXiv:2303.12853 [cs].
- [16] J. Gilmer, S. S. Schoenholz, P. F. Riley, O. Vinyals, and G. E. Dahl, in *Proceedings of the 34th International Conference on Machine Learning* (PMLR, 2017) pp. 1263–1272, iSSN: 2640-3498.
- [17] I. Batatia, D. P. Kovács, G. N. C. Simm, C. Ortner, and G. Csányi, *MACE: Higher Order Equivariant Message Passing Neural Networks for Fast and Accurate Force Fields* (2023), arXiv:2206.07697 [cond-mat, physics:physics, stat].
- [18] C. Chen and S. P. Ong, *Nature Computational Science* **2**, 718 (2022), publisher: Nature Publishing Group.
- [19] B. Deng, P. Zhong, K. Jun, J. Riebesell, K. Han, C. J. Bartel, and G. Ceder, *Nature Machine Intelligence* **5**, 1031 (2023), publisher: Nature Publishing Group.
- [20] I. Batatia, P. Benner, Y. Chiang, A. M. Elena, D. P. Kovács, J. Riebesell, X. R. Advincula, M. Asta, M. Avaylon, W. J. Baldwin, F. Berger, N. Bernstein, A. Bhowmik, S. M. Blau, V. Cáraro, J. P. Darby, S. De, F. Della Pia, V. L. Deringer, R. Elijošius, Z. El-Machachi, F. Falcioni, E. Fako, A. C. Ferrari, A. Genreith-Schriever, J. George, R. E. A. Goodall, C. P. Grey, P. Grigorev, S. Han, W. Handley, H. H. Heenen, K. Hermansson, C. Holm, J. Jaafar, S. Hofmann, K. S. Jakob, H. Jung, V. Kapil, A. D. Kaplan, N. Karimitari, J. R. Kermode, N. Kroupa, J. Kullgren, M. C. Kuner, D. Kuryla, G. Liepuoniute, J. T. Margraf, I.-B. Magdäu, A. Michaelides, J. H. Moore, A. A. Naik, S. P. Niblett, S. W. Norwood, N. O'Neill, C. Ortner, K. A. Persson, K. Reuter, A. S. Rosen, L. L. Schaaf, C. Schran, B. X. Shi, E. Sivonxay, T. K. Stenczel, V. Svahn, C. Sutton, T. D. Swinburne, J. Tilly, C. van der Oord, E. Varga-Umbrich, T. Vegge, M. Vondrák, Y. Wang, W. C. Witt, F. Zills, and G. Csányi, *A foundation model for atomistic materials chemistry* (2024), arXiv:2401.00096 [cond-mat, physics:physics].
- [21] Y. Park, J. Kim, S. Hwang, and S. Han, *Journal of Chemical Theory and Computation* **20**, 4857 (2024), publisher: American Chemical Society.
- [22] H. Yang, C. Hu, Y. Zhou, X. Liu, Y. Shi, J. Li, G. Li, Z. Chen, S. Chen, C. Zeni, M. Horton, R. Pinsler, A. Fowler, D. Zügner, T. Xie, J. Smith, L. Sun, Q. Wang, L. Kong, C. Liu, H. Hao, and Z. Lu, *Mattersim: A deep learning atomistic model across elements, temperatures and pressures* (2024), arXiv:2405.04967 [cond-mat.mtrl-sci].
- [23] A. Dunn, Q. Wang, A. Ganose, D. Dopp, and A. Jain, *npj Computational Materials* **6**, 138 (2020).
- [24] J. Riebesell, R. E. A. Goodall, P. Benner, Y. Chiang, B. Deng, A. A. Lee, A. Jain, and K. A. Persson, *Matbench Discovery – A framework to evaluate*

machine learning crystal stability predictions (2024), arXiv:2308.14920 [cond-mat].

[25] A. Dunn, Q. Wang, A. Ganose, D. Dopp, and A. Jain, *npj Computational Materials* **6**, 138 (2020).

[26] H. Yu, M. Giantomassi, G. Materzanini, J. Wang, and G.-M. Rignanese, Systematic assessment of various universal machine-learning interatomic potentials (2024), arXiv:2403.05729 [cond-mat].

[27] B. Deng, Y. Choi, P. Zhong, J. Riebesell, Z. Li, K. Jun, K. A. Persson, and G. Ceder, Overcoming systematic softening in universal machine learning interatomic potentials by fine-tuning (2024), arXiv:2405.07105.

[28] H. Lee, V. I. Hegde, C. Wolverton, and Y. Xia, Accelerating High-Throughput Phonon Calculations via Machine Learning Universal Potentials (2024), arXiv:2407.09674 [cond-mat].

[29] G. Fugallo, M. Lazzeri, L. Paulatto, and F. Mauri, *Phys. Rev. B* **88**, 045430 (2013).

[30] A. Togo, L. Chaput, and I. Tanaka, *Phys. Rev. B* **91**, 094306 (2015).

[31] A. Seko, A. Togo, H. Hayashi, K. Tsuda, L. Chaput, and I. Tanaka, *Physical Review Letters* **115**, 205901 (2015).

[32] T. Tadano, Y. Gohda, and S. Tsuneyuki, *Journal of Physics: Condensed Matter* **26**, 225402 (2014).

[33] J. Carrete, B. Vermeersch, A. Katre, A. van Roekeghem, T. Wang, G. K. Madsen, and N. Mingo, *Computer Physics Communications* **220**, 351 (2017).

[34] M. Simoncelli, N. Marzari, and F. Mauri, *Nature Physics* **15**, 809 (2019).

[35] M. Simoncelli, N. Marzari, and F. Mauri, *Physical Review X* **12**, 041011 (2022).

[36] M. Simoncelli, F. Mauri, and N. Marzari, *npj Computational Materials* **9**, 1 (2023).

[37] F. Knoop, T. A. Purcell, M. Scheffler, and C. Carbogno, *Physical Review Letters* **130**, 236301 (2023).

[38] A. Jain, S. P. Ong, G. Hautier, W. Chen, W. D. Richards, S. Dacek, S. Cholia, D. Gunter, D. Skinner, G. Ceder, and K. A. Persson, *APL Materials* **1**, 011002 (2013).

[39] R. Peierls, *Annalen der Physik* **395**, 1055 (1929).

[40] S.-i. Tamura, *Phys. Rev. B* **27**, 858 (1983).

[41] M. Simoncelli, N. Marzari, and A. Cepellotti, *Phys. Rev. X* **10**, 011019 (2020).

[42] J. Dragašević and M. Simoncelli, arXiv:2303.12777 (2023).

[43] Y. Liu, H. Liang, L. Yang, G. Yang, H. Yang, S. Song, Z. Mei, G. Csányi, and B. Cao, *Advanced Materials* **35**, 2210873 (2023).

[44] A. F. Harper, K. Iwanowski, W. C. Witt, M. C. Payne, and M. Simoncelli, *Physical Review Materials* **8**, 043601 (2024), publisher: American Physical Society.

[45] E. Di Lucente, M. Simoncelli, and N. Marzari, *Physical Review Research* **5**, 033125 (2023).

[46] A. Jain, *Phys. Rev. B* **102**, 201201 (2020).

[47] M. Simoncelli, D. Fournier, M. Marangolo, E. Balan, K. Béneut, B. Baptiste, B. Doisneau, N. Marzari, and F. Mauri, Temperature-invariant heat conductivity from compensating crystalline and glassy transport: from the Steinbach meteorite to furnace bricks (2024), arXiv:2405.13161 [cond-mat].

[48] G. Caldarelli, M. Simoncelli, N. Marzari, F. Mauri, and L. Benfatto, *Physical Review B* **106**, 024312 (2022).

[49] A. Fiorentino and S. Baroni, *Physical Review B* **107**, 054311 (2023).

[50] S. Bandi, C. Jiang, and C. A. Marianetti, *Machine Learning: Science and Technology* (2024).

[51] X. Gonze and C. Lee, *Physical Review B* **55**, 10355 (1997).

[52] J. L. Hintze and R. D. Nelson, *The American Statistician* **52**, 181 (1998).

[53] J. M. Ziman, *Electrons and phonons: the theory of transport phenomena in solids* (Oxford university press, 1960).

[54] A. H. Larsen, J. J. Mortensen, J. Blomqvist, I. E. Castelli, R. Christensen, M. Dułak, J. Friis, M. N. Groves, B. Hammer, C. Hargus, E. D. Hermes, P. C. Jennings, P. B. Jensen, J. Kermode, J. R. Kitchin, E. L. Kolsbjer, J. Kubal, K. Kaasbjer, S. Lysgaard, J. B. Maronsson, T. Maxson, T. Olsen, L. Pastewka, A. Petersen, C. Rostgaard, J. Schiøtz, O. Schütt, M. Strange, K. S. Thygesen, T. Vegge, L. Vilhelmsen, M. Walter, Z. Zeng, and K. W. Jacobsen, *Journal of Physics: Condensed Matter* **29**, 273002 (2017).

[55] A. Togo, L. Chaput, T. Tadano, and I. Tanaka, *Journal of Physics: Condensed Matter* **35**, 353001 (2023), publisher: IOP Publishing.

[56] Y. Wang, J. J. Wang, W. Y. Wang, Z. G. Mei, S. L. Shang, L. Q. Chen, and Z. K. Liu, *Journal of Physics: Condensed Matter* **22**, 202201 (2010).

[57] X. Gonze and C. Lee, *Physical Review B* **55**, 10355 (1997).

[58] A. Togo, *Journal of the Physical Society of Japan* **92**, 012001 (2023).

[59] J. P. Perdew, K. Burke, and M. Ernzerhof, *Physical Review Letters* **77**, 3865 (1996).

[60] T. W. Ko, M. Nassar, S. Miret, E. Liu, and S. P. Ong, *Materials graph library* (2023).

[61] S. Plimpton, *Journal of Computational Physics* **117**, 1 (1995).